Kovove Mater. 62 2024 181–196
DOI: 10.31577/km.2024.3.181

Study on corrosion behavior of Sb-Sn high-strength weathering steel under simulated industrial atmospheric environment

Yun-Long Wang[1], Guo-Hua Ding[1], Li-Meng Liang[2], Xiao-Ri Dong[1], Chun-Jing Liu[1,2]*

[1] *School of Mechanical and Vehicular Engineering, Bengbu University, Bengbu 233030, P. R. China*
[2] *Anhui Engineering Research Center of Additive Manufacturing, Bengbu 233030, P. R. China*

Received 20 May 2024, received in revised form 24 June 2024, accepted 3 July 2024

Abstract

In this paper, Sb and Sn elements were added to high-strength weathering steel. The corrosion behavior of three kinds of high-strength weathering steels without Sb/Sn, with Sb and Sb + Sn in a simulated industrial atmosphere, was studied. The results show that adding Sb and Sn can accelerate the initial corrosion rate, quickly form a more dense and stable rust layer, and thus reduce the corrosion rate and total corrosion amount in the later period. Sb and Sn are uniformly distributed in the rust layer and play an important role in improving the density of the rust layer. The corrosion resistance of weathering steel is improved after the addition of Sb alone and Sb + Sn combined, and the corrosion resistance is more excellent when the composite is added.

K e y w o r d s: weathering steel, corrosion, simulated industrial atmosphere, rust layer, corrosion mechanism

1. Introduction

By adding a small number of alloying elements, such as Cu, Cr, Ni, Si, Mn, etc., these alloying elements are enriched in the rust layer so that the rust layer of the weathering steel is obviously denser than that of carbon steel, and the corrosion resistance is 2–8 times higher than that of carbon steel [1–3]. The development of high-performance weathering steel from the initial Corten series to the present includes not only the improvement of corrosion resistance but also the optimization and upgrading of mechanical properties, making weathering steel widely used in railway vehicles, ships, bridges, and other engineering fields [4–7].

By optimizing the proportion of alloy elements, the researchers can improve the corrosion resistance as much as possible based on satisfying the mechanical properties. Adding a small amount of Sb element to traditional weathering steel can enhance the corrosion resistance of weathering steel in sulfuric acid, nitric acid, and hydrochloric acid [8–10]. The Sb element is a beneficial element for improving corrosion resistance. In the 1960s, Japanese iron and steel companies developed steel containing C, Si, Mn, P, S, Cu, and Sb and found that the steel had excellent resistance to sulfuric acid dew point corrosion [8]. The Sn element has been used for a long time in the steel industry, mainly in the intermediate phase and solid solutions, and is generally considered an element harmful to steel. However, according to scholars' reports, Sn may be beneficial for improving corrosion resistance. Liu Bo et al. [11] confirmed that adding Sn can significantly inhibit the cathode H+ reduction reaction under acidic conditions and make the steel matrix more resistant to atmospheric corrosion. Ahn, Soo Hoon, et al. [12] found that the protective corrosion products SnO_2 and Sb_2O_5 produced by micro-alloyed steels containing Sn and Sb in acidic chloride corrosion media can act as inhibitors of anode reaction. In addition, the synergistic interaction between Sb, Sn, Cu, and other elements is also very helpful in improving corrosion resistance, and a continuous dense Sn-Sb-Cu oxide layer can be generated to protect the matrix [13, 14].

Sb element is a newly discovered microalloying element that has been conducive to improving the corrosion resistance of low-alloy, high-strength steel in recent years, and its content is usually not more than

*Corresponding author: e-mail address: liusun7575@163.com

Table 1. The chemical composition of three weathering steels (mass fraction (%))

Steels	C	Si	Mn	P	S	Cu	Cr	Ni	Sb	Sn	Nb	Ti
Sb/Sn-free steel	0.071	0.26	0.84	0.006	0.003	0.36	0.75	0.48	–	–	0.044	0.024
Sb steel	0.083	0.26	0.91	0.006	0.003	0.37	0.76	0.47	0.050	–	0.044	0.025
Sb + Sn steel	0.059	0.23	0.84	0.0086	0.0005	0.36	0.84	0.19	0.098	0.022	0.036	0.027

Table 2. Mechanical properties of three experimental steels

	Yield strength, R_{el} (MPa)	Tensile strength, R_m (MPa)	Elongation after breaking, A (%)
Sb/Sn-free steel	519	620	31.1
Sb steel	552	655	29.2
Sb + Sn steel	537	635	30.5

0.1 %, which can affect the recrystallization process and acid corrosion resistance of low-alloy structural steel. In 2004, Japan Nippon Steel Company found for the first time that adding an appropriate amount of Sb to Cu-containing steel could promote the formation of Cu_2Sb film, inhibit the electrochemical anode and cathode reaction, and significantly improve the corrosion resistance of low alloy steel to sulfuric acid and hydrochloric acid [15]. The study of South Korean scholar Le [16] confirmed that adding trace Sb element can improve the corrosion resistance of low-alloy steel in the mixed environment of sulfuric acid and hydrochloric acid. 0.1%Sb element could not only produce a protective Sb_2O_5 oxide film on the surface but also accelerated the formation of Cu-containing compounds in the product film, significantly inhibiting the electrochemical anode [17, 18] and cathode reaction through the interaction of Sb and Cu, and reduce the corrosion current density [19].

Most scholars have only studied the corrosion behavior of singly added Sb or Sn, and the yield strength of its weathering steel is mostly below 450 MPa [20]. To promote the application field of weathering steel, we have developed a new generation of high-strength weathering steel (above 500 MPa level) by adjusting the element ratio and adding Sb and Sn elements separately and composite. By simulating the industrial atmospheric corrosion environment, the corrosion mechanism of high-strength weathering steel in $NaHSO_3$ solution is deeply discussed. At the same time, the role of Sb, Sn, and other elements in the rust layer is also studied, which has a certain reference significance for the upgrading of weathering steel.

2. Experimental materials and methods

2.1. Experimental materials

The weathering steel used in the experiment was refined by the vacuum smelting furnace of Shougang Technology Research Institute, and a three-square ingot of 65 mm × 65 mm × 65 mm weathering steel was obtained by forging. The chemical composition is shown in Table 1. After forging, the process parameters of hot rolling are controlled by rolling and cooling. The billet is heated to 1200 ℃ and kept warm for 2 hours. The rolling temperature of rough rolling is 1150 ℃, and the rolling temperature of final rolling is 1050 ℃. Finishing rolling temperature 950 ℃, rolling 3 times, final rolling temperature 850 ℃. The thickness of each roll is 65 mm → 53 mm → 41 mm → 31 mm → 23 mm → 15.5 mm → 10.5 mm → 7.5 mm, and the reduction rate is as follows: 18.5, 22.6, 24.4, 25.8, 32.6, 32.3, 33.3, and 28.6 %, the total deformation of 88.5 %. Rolling controls the cooling process, cooling to 570 ℃, cooling speed of 5–8 ℃ s^{-1}. The material is then placed in a resistance furnace for further cooling to room temperature.

The metallographic structure of the three experimental steels is shown in Fig. 1, which is mainly composed of ferrite and pearlite. It can be seen from the figure that the metallographic structure, grain size, and distribution of the three kinds of steel are basically the same, so the influence of metallographic structure on corrosion can be ignored. The mechanical properties of the three kinds of steel are shown in Table 2. The lower yield strength and tensile strength of the three kinds of experimental steel all exceed 500 MPa, and the elongation after breaking is about 30 %. The mechanical properties of the experimental steel are relatively excellent.

2.2. Experimental methods

According to railway industry standard TB/T2375-1993 "*Test Method for Periodic Infiltration and Corrosion of Weathering Resistant Steel for Railway*," the test experiment was carried out to simulate the corrosion environment of an industrial atmosphere. The

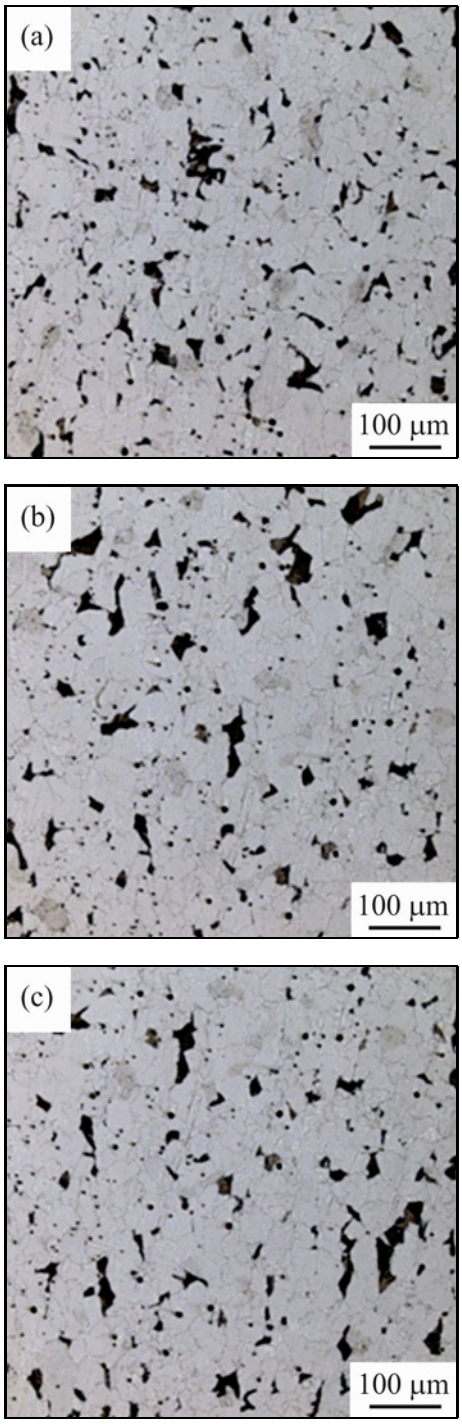

Fig. 1. Metallographic structure of three experimental steels: (a) Sb/Sn-free steel, (b) Sb steel, and (c) Sb + Sn steel.

infiltrating solution was 1.0×10^{-2} mol L^{-1} $NaHSO_3$ solution, the test temperature was 45 ± 2 ℃, and the relative humidity was 70 ± 5 % RH. One cycle was 60 min (wetting 12 min, drying 48 min), and the test cycle nodes were set as 24, 72, 120, and 168 h. The sample size was 60 mm × 40 mm × 2 mm, and three parallel samples were set up in each cycle. After the experiment, a hydrochloric acid solution with a corrosion inhibitor dedusted the samples and lost weight. After cleaning, drying, and weighing, the average corrosion rate (g m^{-2} h^{-1}) was calculated.

The surface morphology of the samples was observed by Qutanta FEG450 thermal field emission environmental scanning electron microscope. The cross-section of the rust layer was observed by an Olympus OLS4100 confocal laser microscope (CLSM). To observe the phase evolution of the rust, XRD measurements were made with a D8 Advance X-ray diffractometer using a copper X-ray tube and diffracted beam monochromator, which collected data in the range of 2θ angle of 10°–90° at a scanning rate of 2° min^{-1} and a scanning step of 0.02. The Electro-Probe Microanalyzer (EPMA) instrument model JXA8100 is used to observe the distribution of elements in the rust layer, with an acceleration voltage of 20 kV, emission current of 1×10^{-8} A, and spot diameter of 1 μm.

The electrochemical test of bare steel and rust samples was carried out at the RST electrochemical workstation. SCE is used as the reference electrode, and the auxiliary electrode is an extremely bright platinum (Pt) electrode, and the electrode potentials in this paper are relative to the auxiliary electrode. The test solution was 0.01 mol L^{-1} $NaHSO_3$ + 3.5 % NaCl mixed solution. The working surface of the electrochemical sample is 10 mm × 10 mm. The corresponding non-working surface is welded with copper wire by tin welding, and the rest is encapsulated with epoxy resin. After drying, the working surface of the sample is fine ground to 2000# sandpaper and then put into the periodic infiltration accelerated corrosion test chamber. Bare steel and rust samples completed the periodic infiltration corrosion test and could be directly subjected to electrochemical experiments. The polarization curve test has a scanning rate of 0.5 mV s^{-1} and a scanning voltage range of ± 0.5 V (relative to the open circuit potential). The electrochemical impedance spectroscopy test was carried out under the self-etching potential, the AC disturbance voltage amplitude was 10 mV, and the scanning frequency range was 1×10^{-2}–1×10^{5} Hz.

3. Results and analysis

3.1. Rule of corrosion weightlessness

Figure 2 shows the relationship between corrosion weight loss rate and time of Sb/Sn free steel, Sb steel, and Sb + Sn steel after periodic infiltration corrosion test. It can be seen from the figure that with the increase in corrosion time, the corrosion rate of the three kinds of steel shows a trend of decreasing, and the

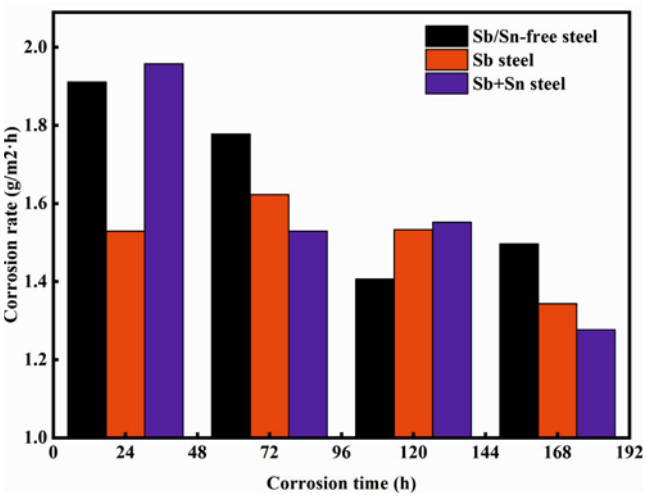

Fig. 2. Corrosion weight loss diagram of three steels.

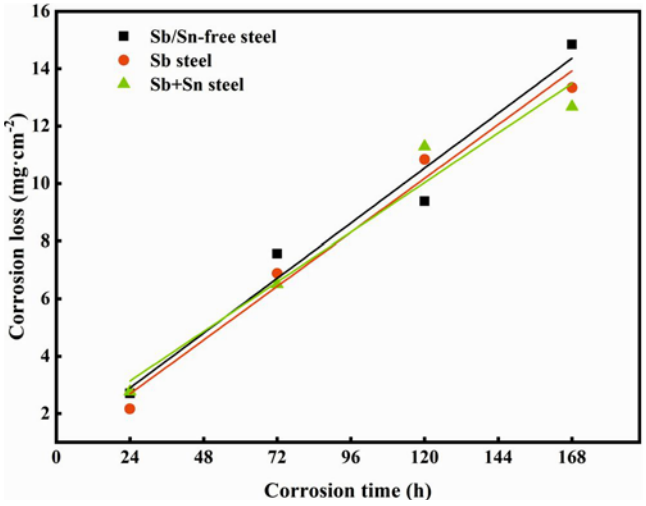

Fig. 3. Corrosion weight loss fitting curves of three steels.

Table 3. Linear fitting parameters in Fig. 3

	Linear fitting parameters
Sb/Sn-free steel	$y = 0.0796x + 0.9821;\ R^2 = 0.9536$
Sb steel	$y = 0.0780x + 0.9737;\ R^2 = 0.9737$
Sb + Sn steel	$y = 0.0719x + 1.4101;\ R^2 = 0.9424$

corrosion weight loss rate is not different. To explain the relationship between the corrosion rate and corrosion resistance of the three steels, the corrosion weight loss curves of the three steels are fitted in Fig. 3, and the fitting regression parameters are shown in Table 3. From the figure, it is evident that the corrosion weight loss of the three steels increases with time. Compared with the steel without Sb/Sn, the curves of Sb steel and Sb + Sn steel show a more similar trend. When the corrosion time is less than or equal to 120 h, it belongs to the pre- and mid-stage corrosion. The corrosion weight loss of the three kinds of steel fluctuates constantly, and a stable corrosion rust layer has not yet formed. However, when the corrosion time reaches 168 h, it belongs to the middle and late stage of corrosion, at which time a stable rust layer has formed, and the dense and stable rust layer becomes an effective barrier between the material substrate and the external corrosion environment, which can hinder the further development of corrosion and better reflect the comprehensive corrosion resistance of the material. At 168 h, the corrosion rate of Sb steel and Sb + Sn steel decreased significantly, and it can be seen from Fig. 3 that Sb + Sn steel can preferentially form a stable rust layer. This is related to adding trace amounts of Sb and Sn elements. According to relevant reports, the protective corrosion products SnO_2 and Sb_2O_5 can be generated by the microalloyed steel containing Sn and Sb, or it can cooperate with Cu to make the rust layer denser [18, 19].

3.2. Analysis of microscopic corrosion morphology

Figure 4 shows the Sb + Sn steel microstructure under different corrosion periods. The steel surface is uniformly covered with fine corrosion products. To the right of Figs. 4a–h is a partially enlarged view in the yellow rectangle on the left. For weathering steel, the surface morphology shows a flowery flock-like microstructure, which is typical of gamma-FeOOH crystal grains, while the three-dimensional spheroidal ("cotton spheroidal") structure corresponds to the typical microscopic characteristics of α-FeOOH [21]. It can be seen from the figure that there are large differences in the corrosion morphology under different corrosion periods. At the initial corrosion stage (24 h), there are more flocculated γ-FeOOH grains, but due to the short corrosion period, the spherical α-FeOOH grains have not been fully formed, so there are no obvious spherical particles in the micro-morphology. After 72 h of corrosion, the spherical particles began to appear, and the floccus structure began to decrease. After 120 h of corrosion, spherical α-FeOOH particles were formed, the number increased significantly, and the floccus structure became less. The surface had mainly spherical particles after 168 h in the corrosion stage, and the floor-flocculent structure disappeared. According to the above analysis, with the extension of the corrosion period, the content of α-FeOOH in the ball increased significantly, while the content of γ-FeOOH in the floc gradually decreased.

Figure 5 shows the micromorphology of the three steel kinds after 168 h corrosion. The microscopic sur-

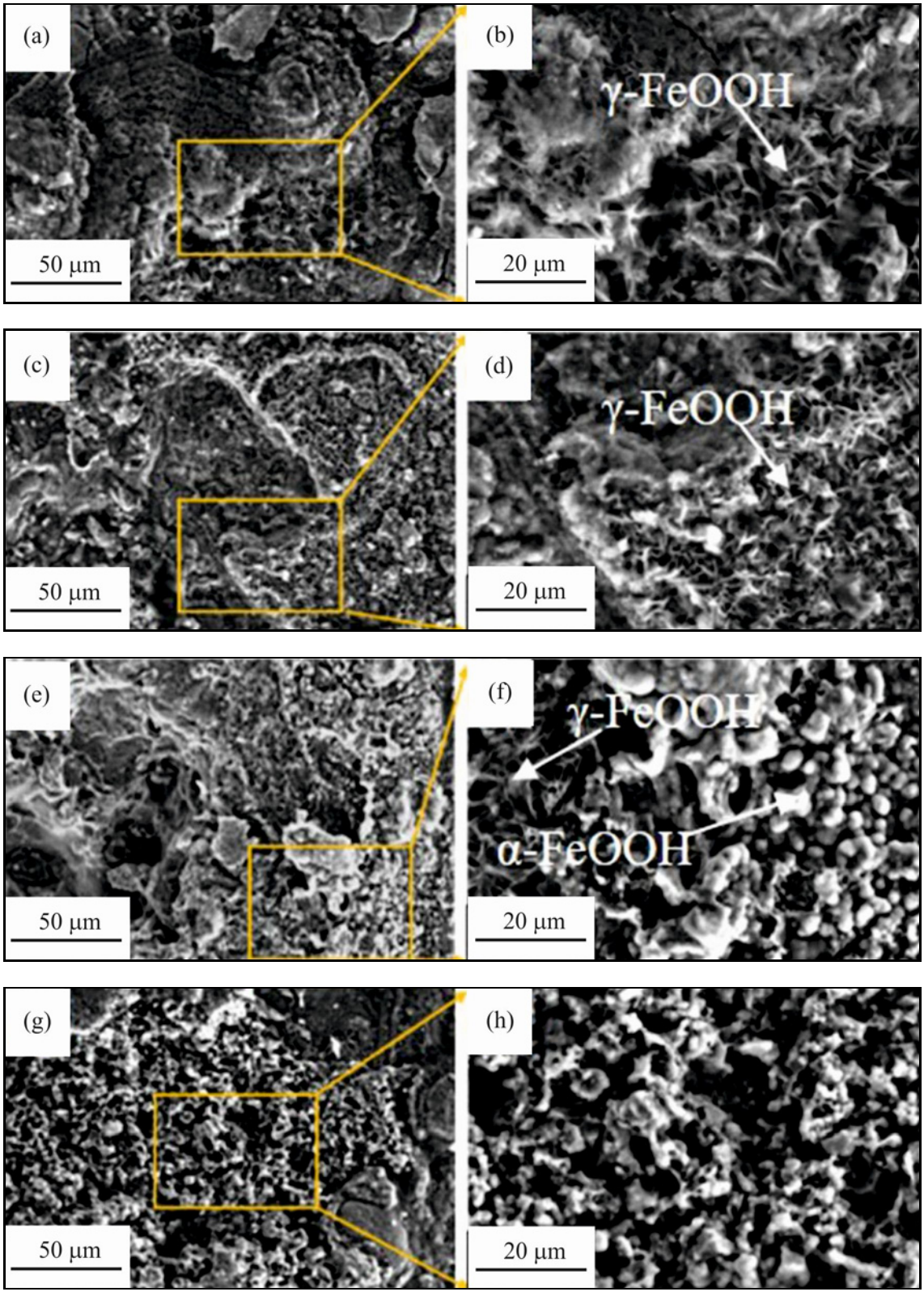

Fig. 4. Micro-morphology of Sb + Sn steel under different corrosion cycles: (a), (b) 24 h; (c), (d) 72 h; (e), (f) 120 h; and (g), (h) 168 h.

faces of the three kinds of steel have relatively similar characteristics, mainly composed of balls or blocks and a small amount of cotton-like structure. Cracks occur on the rust layer on the surface, but the cracks of Sb

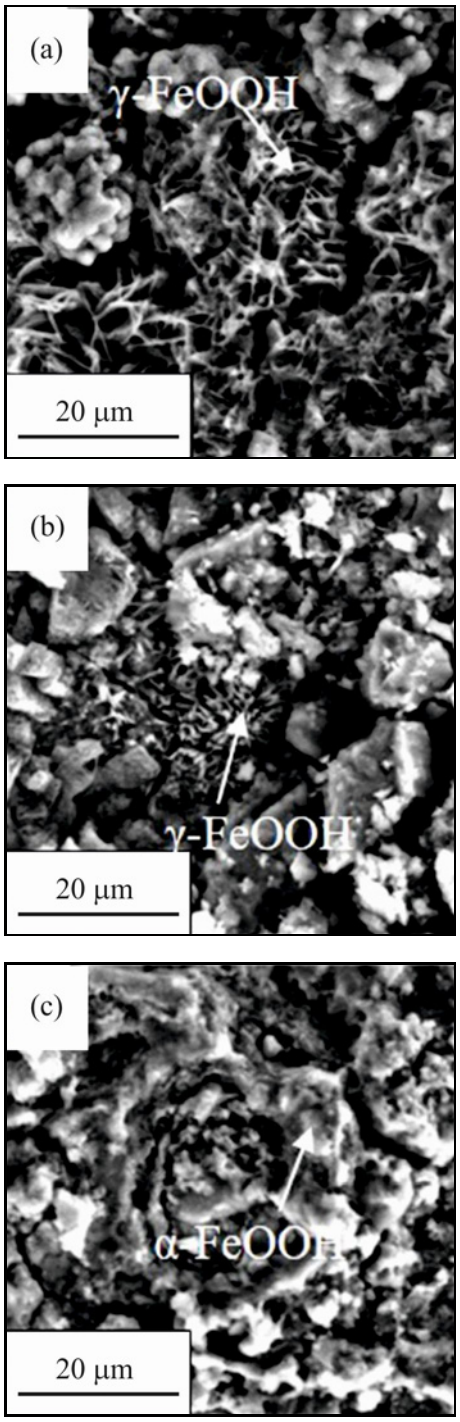

Fig. 5. Micro-morphology of the three steels after 168 h corrosion: (a) Sb/Sn-free steel, (b) Sb steel, and (c) Sb + Sn steel.

steel and Sb + Sn steel are finer than those of steel without Sb/Sn, which indicates that the rust layer of Sb steel and Sb + Sn steel is denser and has a stronger protective effect on the matrix.

Figure 6 shows the morphology of the cross-section rust layer of Sb/Sn free steel, Sb steel, and Sb + Sn steel. On the left (white) is the steel substrate (Sub), in the middle is the rust layer, and on the right (dark) is the epoxy resin cold insert (EP). The thickness of the rust layer of the three kinds of steel increases gradually with the extension of corrosion time. From the point of view of corrosion time: In the early stage of corrosion (24 h), the steel surface begins to be destroyed, forming a small amount of rust layer, so the corrosion of the rust layer is thinner. However, due to the non-uniformity of corrosion, there is local pitting corrosion, as shown in Fig. 6e – 24 h. Combined with Fig. 4, it can be inferred that the early stage of corrosion is dominated by small-hole corrosion. When the small holes on the metal surface are gradually connected, they are transformed into more uniform corrosion. In the middle stage of corrosion (72–120 h), the rust layer gradually becomes thicker, and there are obvious cracks between the inner and outer rust layers. The thickness of the outer rust layer is larger than that of the inner rust layer, indicating that the stable structure of the inner rust layer has not been formed at this time. In the later stage of corrosion (168 h), the yellowish-brown part is the outer rust layer, and the gray and white part is the inner rust layer. The inner rust layer is already very dense, and the cracks are greatly reduced. The thickness of the inner rust layer is relatively uniform, which can effectively hinder the further development of corrosion.

3.3. Analysis of corrosion products

Figure 7 shows the XRD patterns of the oxide rust layer on the surface of three kinds of steel. The main oxides in the figure are Fe_2O_3, Fe_3O_4, α-FeOOH, and γ-FeOOH. Among them, Fe_2O_3 is a reddish-brown powder, mainly distributed in the outermost part of the rust layer, and has a large grain size, which can reduce the adhesion of the rust layer and does not have protection for the matrix. Fe_3O_4 is a good conductor with stable thermodynamic properties and a dense structure. The thermodynamic properties of α-FeOOH are the most stable [22, 23]; the grain is thin, and the rust layer is dense, which is the main component of the inner rust layer and has a good protective effect on the matrix. In general, the higher the content, the stronger the protective effect after forming a stable rust layer. The thermodynamic stability of γ-FeOOH is poor, mainly distributed in scales in the outer rust layer, and loose porous γ-FeOOH can be transformed into stable α-FeOOH.

With the prolongation of the corrosion period, the intensity of the diffraction peak in the figure changes somewhat. The intensity of the diffraction peak mainly reflects the abundance of the corresponding crystalline phase, and the particle size or crystallinity is related to the width of the diffraction peak. Figure 7a shows that in Sb/Sn free steel, the diffrac-

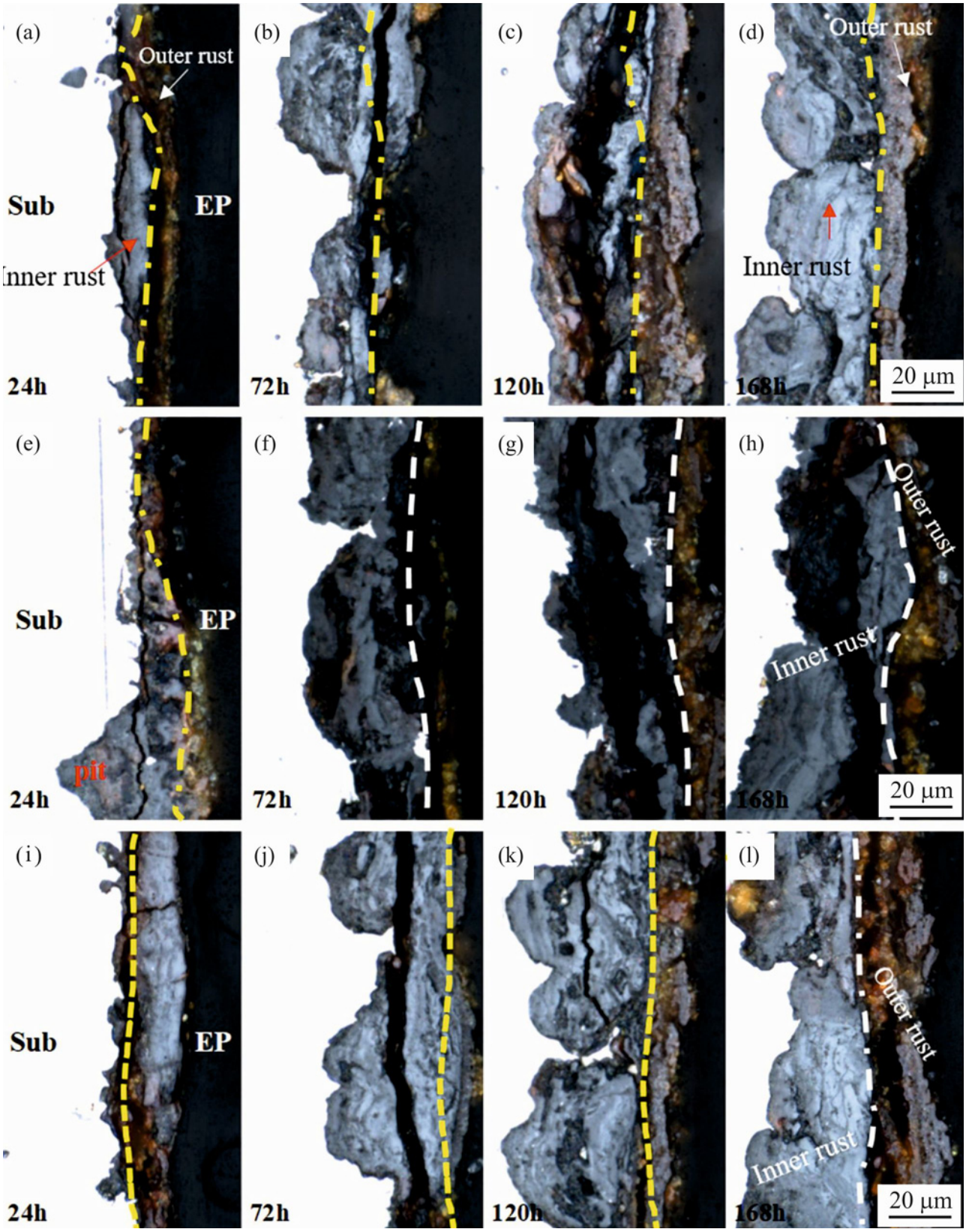

Fig. 6. Cross-sectional rust layer morphology of three steels under different corrosion cycles: (a)–(d) Sb/Sn-free steel, (e)–(h) Sb steel, and (i)–(l) Sb + Sn steel.

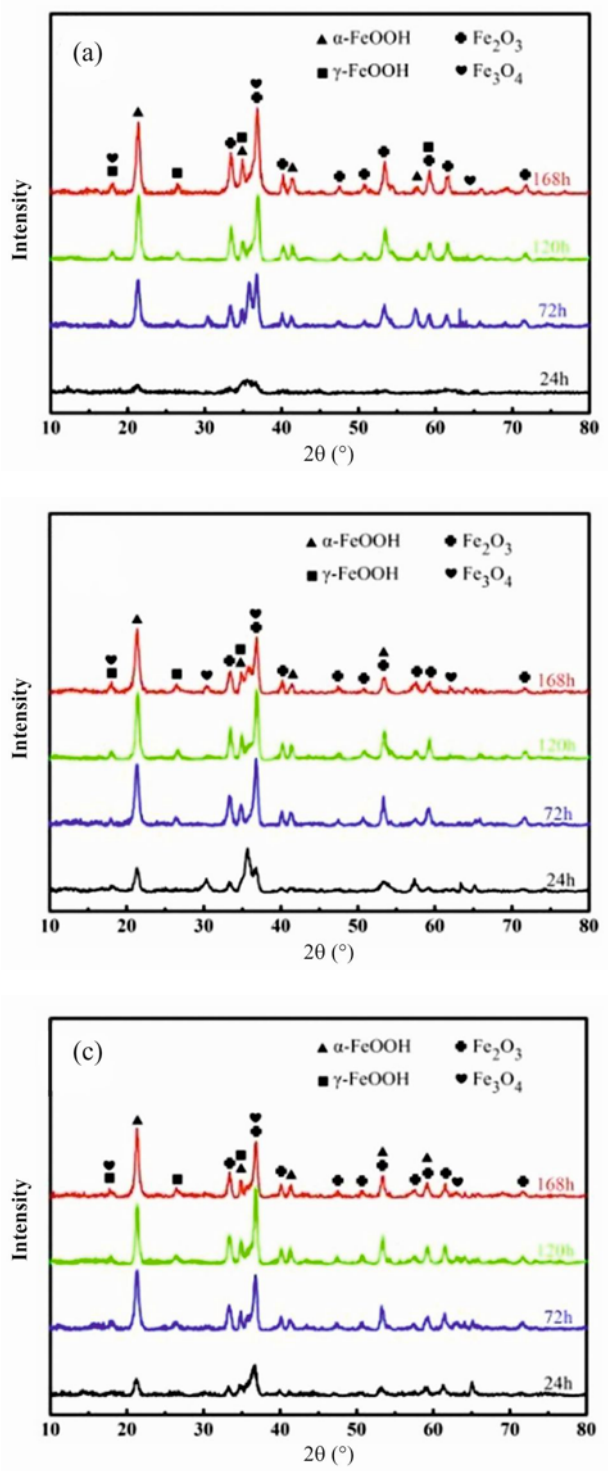

Fig. 7. XRD patterns of oxide scales on the surface of three types of steel: (a) Sb/Sn-free steel, (b) Sb steel, and (c) Sb + Sn steel.

tion peak intensity of α-FeOOH gradually increased, and the diffraction peaks of Fe_2O_3 and Fe_3O_4 also increased slightly. However, the diffraction peak patterns in Figs. 7b,c show that the diffraction peak intensity of Fe_2O_3 and Fe_3O_4 decreases after corrosion for 168 h compared with 72 and 120 h. This indicates that the volume proportion of Fe_2O_3 and Fe_3O_4 decreases while the volume content of α-FeOOH gradually increases.

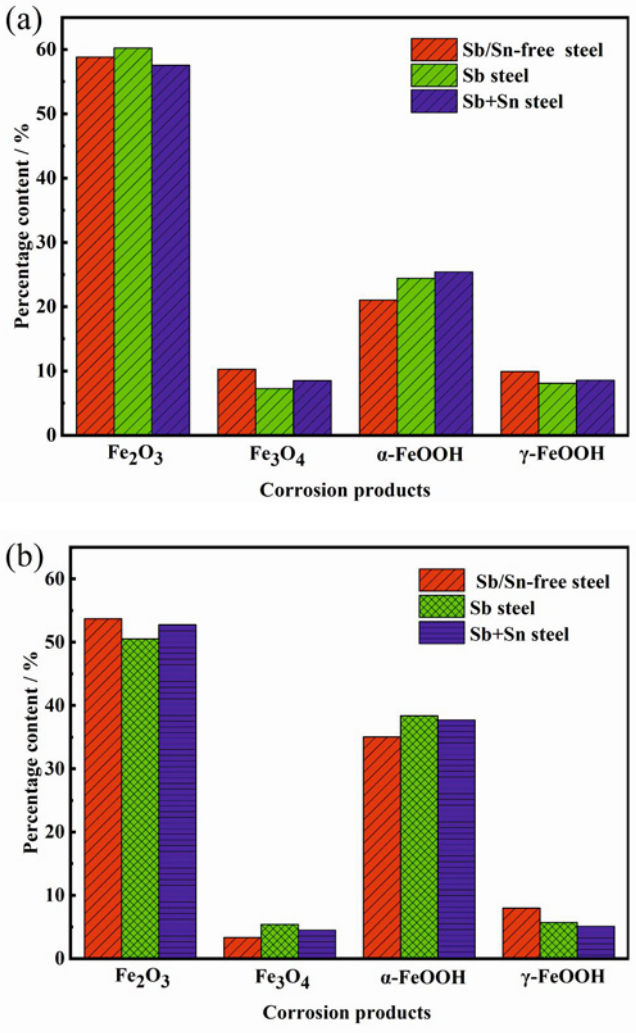

Fig. 8. The relative content of 24 h and 168 h corrosion products of three steels: (a) 24 h and (b) 168 h.

Figure 8 shows the relative content of corrosion products of the three steels with corrosion periods of 24 and 168 h. The most important corrosion products are Fe_2O_3 and α-FeOOH while containing a small amount of Fe_3O_4 and γ-FeOOH. Compared with the content proportion of corrosion products in Figs. 8a,b, Fe_2O_3, Fe_3O_4, and γ-FeOOH contents are higher in the initial corrosion stage (24 h), while the protective α-FeOOH content increases in the later corrosion stage (168 h), and the protective effect on the matrix is improved with the formation of stable rust layer. Compared with non-Sb/Sn steel, the content of α-FeOOH in Sb steel and Sb + Sn steel is higher, and the corrosion resistance of the rust layer is better, which may

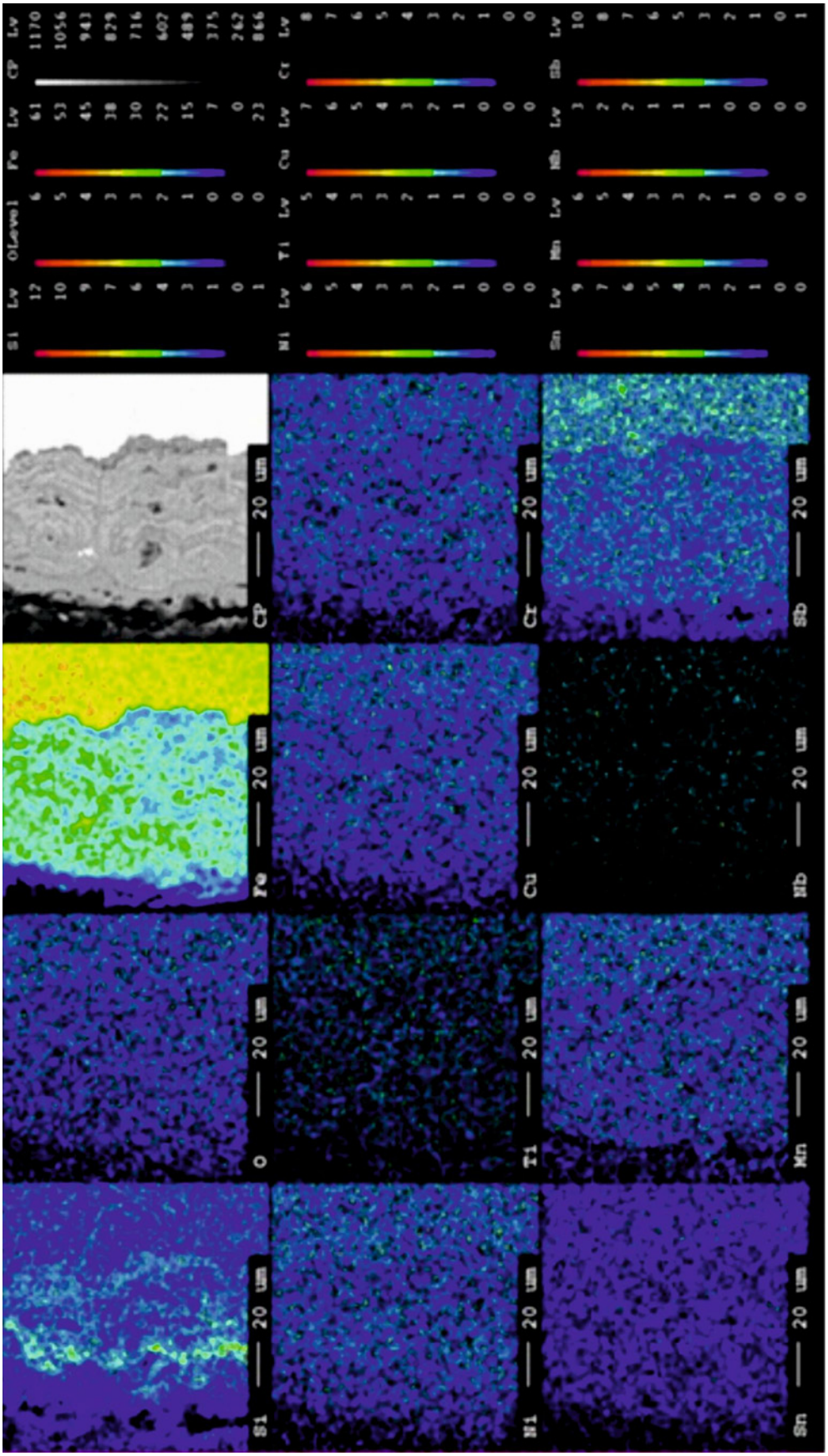

Fig. 9. EPMA surface scan spectrogram of rust section of Sb + Sn steel.

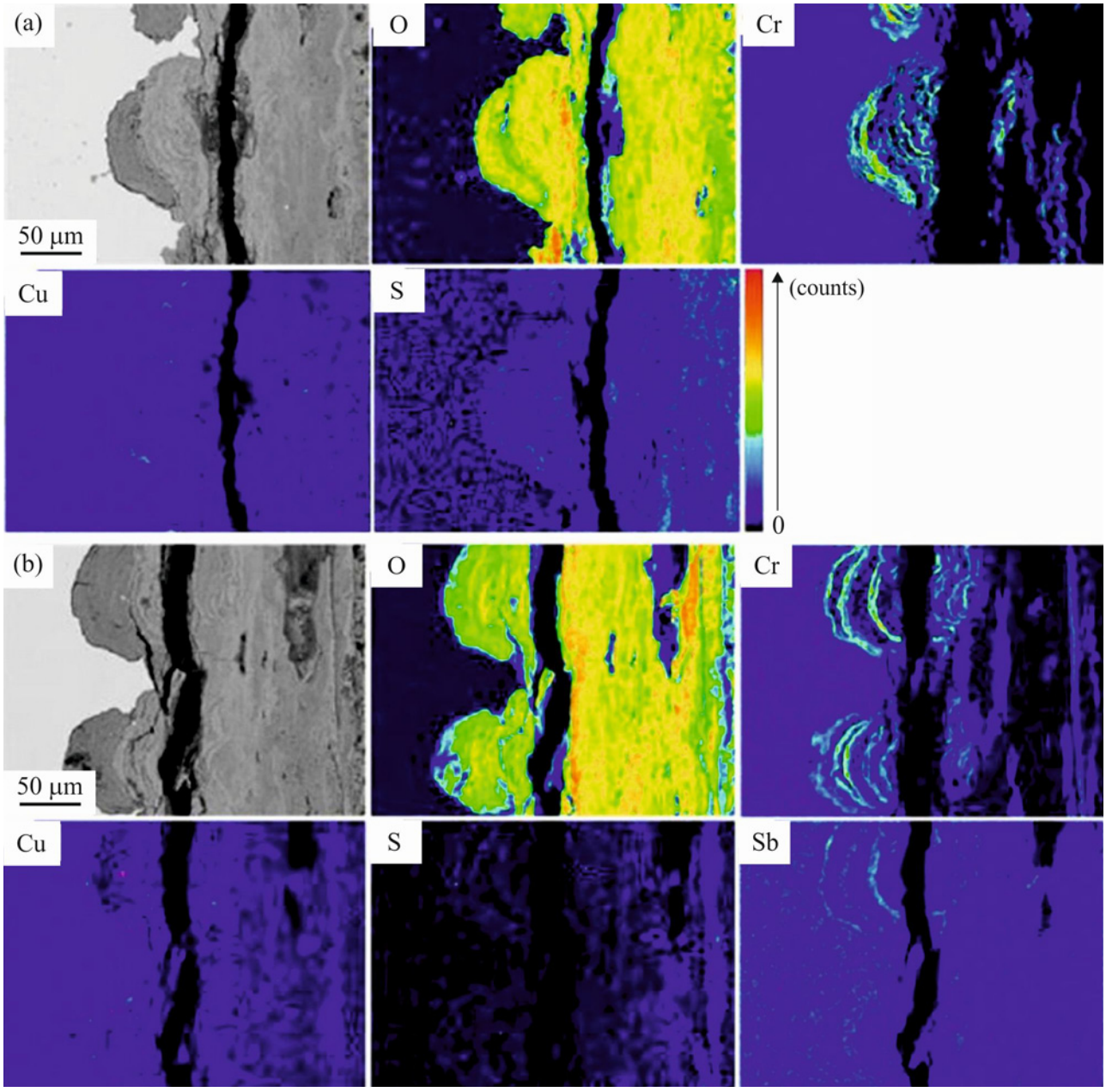

Fig. 10. EPMA surface scan spectrogram of rust section of steels: (a) Sb/Sn free steel and (b) Sb steel.

be related to Sb and Sn elements and can promote more transformation of the rust layer to α-FeOOH, but the specific mechanism is not clear.

3.4. Element distribution in the rust layer

Figure 9 shows the EPMA face scan diagram of Sb + Sn steel. In the original image, the darkest black area on the left is epoxy resin, the middle gray area is the rust layer, and the far-right area is the steel matrix. The figure shows that the content of Fe in the rust layer is significantly lower than that in the matrix, while the content of O in the rust layer is increased, which is related to the formation of hydroxyl iron oxide in the rust layer. Cr element is locally enriched in the rust layer, which plays an important role in forming a dense rust layer, mainly in the later stage of corrosion. On the one hand, it can promote the formation of new α-FeOOH, and on the other hand, it can replace part of the Fe element in the hydroxyl iron oxide to form iron-chromium complex hydroxyl oxide [24]. Different scholars have different views on the influence of Ni element on corrosion resistance, but most scholars believe Ni element has a negative effect on resistance. We can see from the atlas that Ni is evenly distributed in the matrix and rust layer, which may have a negative impact on corrosion resistance. The distribution of Cu and Mn in the rust layer is rela-

Table 4. Corrosion voltage and corrosion current of three kinds of steel under different corrosion cycles and bare steel

	Argument	0 h	24 h	72 h	120 h	168 h
Sb/Sn-free steel, Sb steel	E_{corr} (V)	–0.6481	–0.5808	–0.5155	–0.5667	–0.5928
	I_{corr} (mA cm^{-2})	0.0936	0.09204	0.1514	0.1106	0.1206
Sb + Sn steel, Sb/Sn-free steel	E_{corr} (V)	–0.6879	–0.5572	–0.5031	–0.5511	–0.5602
	I_{corr} (mA cm^{-2})	0.1127	0.1213	0.1392	0.1594	0.1175
Sb steel	E_{corr} (V)	–0.6661	–0.5557	-0.5193	-0.5318	–0.5277
	I_{corr} (mA cm^{-2})	0.0976	0.1575	0.1545	0.0976	0.1109

tively uniform, but the content of Cu and Mn in the rust layer is lower than that in the matrix, and it is possible to form a dense oxide layer with copper oxides or with other alloying elements (such as Cu-Sb-Sn oxides). Studies have shown that Mn can increase the content of α-FeOOH and increase the density of the rust layer [25]. Nb is evenly distributed in the rust layer and matrix so that it may play a greater role. On the one hand, Nb can refine the grains and precipitate them on the grain boundaries as Nb (C, N), reducing chromium carbide enrichment on the grain boundaries and reducing the trend of grain boundary corrosion [26]. On the other hand, Nb can improve the stability and densification of the rust layer and increase the resistance of the rust layer [27]. Similarly, Sb and Sn elements are evenly distributed in the rust layer and are mainly uniformly filled in the loose position of the rust layer in the form of metal oxides, making the rust layer denser.

Figure 10 shows the EPMA surface scanning results of Sb/Sn-free steel and Sb steel. Compared with Fig. 9, Cu and Cr elements are enriched in the three kinds of steel, and an obvious enrichment of Sb can be observed in Fig. 10b.

Due to the small content of Sb and Sn elements, the XRD sensitivity is limited, and the presence of Sb/Sn elements in the rust layer is undetected. In this paper, XPS technology is used to detect Sb elements in the rust layer of Sb + Sn experimental steel. Figure 11 shows the detection results of Sb and Sn 3d spectral peaks. Because the binding energy of Sb 3d and O 1s orbits is close, it is easy to be confused, so the experimental results are fitted by peak-splitting. The isolated peaks are FeOOH, Fe_3O_4, Sb_2O_3(529.9 eV), SnO_2, and other substances. Sb exists in the rust layer in the form of Sb_2O_3, Sb_2O_3, and SnO_2 themselves, which have good thermodynamic stability and uniform and dense structure, so the presence in the inner rust layer will improve the structure of the rust layer, promote the solid combination of the rust layer and the matrix, so that the inner rust layer has a stronger

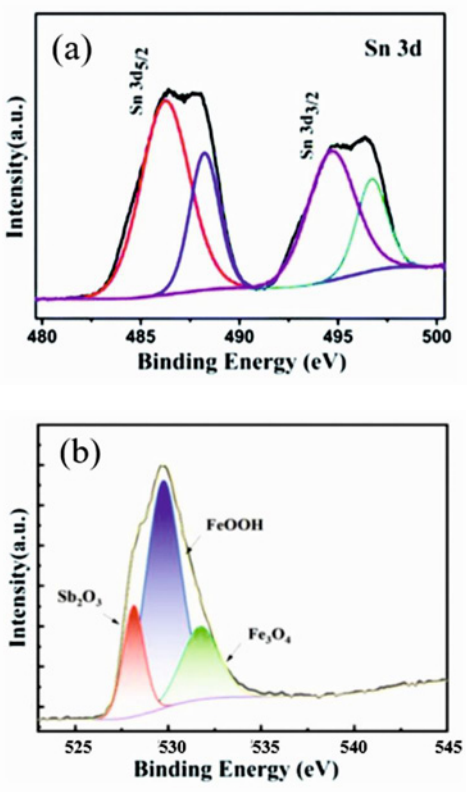

Fig. 11. XPS analysis results of Sb + Sn steel: (a) Sn and (b) Sb.

blocking effect on corrosive ions, thus inhibiting the occurrence of corrosion.

3.5. Electrochemical analysis

Figure 12 describes the polarization curves of bare steel and rust samples of three kinds of steel measured in a mixed solution of 0.01 mol L^{-1} $NaHSO_3$ + 3.5 % NaCl. Self-corrosion potential (E_{corr}) and self-corrosion current (I_{corr}) also change with the change in corrosion time. Table 4 lists the E_{corr} and I_{corr} of

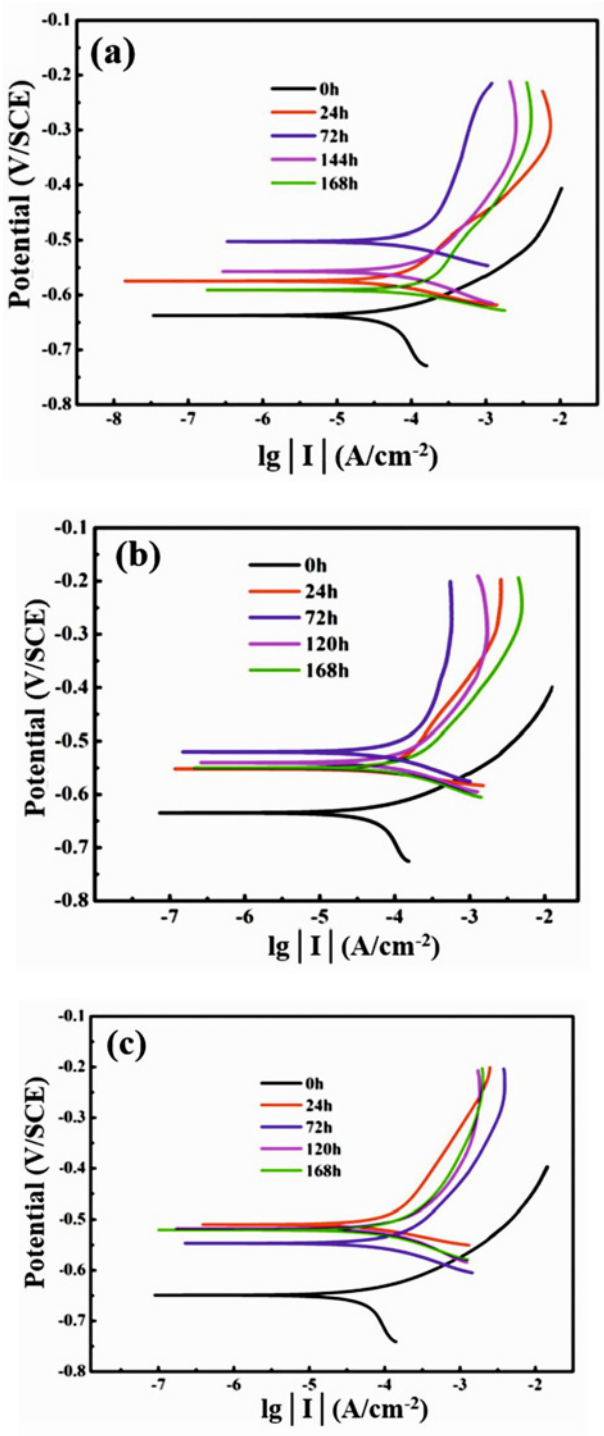

Fig. 12. Polarization curves of three kinds of steel under different corrosion cycles and bare steel: (a) Sb/Sn-free steel, (b) Sb steel, and (c) Sb + Sn steel.

three kinds of steel in different corrosion cycles under a simulated industrial atmospheric corrosion environment. In the electrochemical corrosion process, weathering-resistant steel is controlled by two parts: anodic dissolution reaction and cathodic reduction reaction [28].

For bare steel samples, the anode process is controlled by the dissolution of the steel, and the cathode process is controlled by the reduction of dissolved oxygen. As can be seen from Fig. 12, the self-corrosion potential of the three kinds of bare steel is significantly lower than that of the corroded sample, but as can be seen from Table 4, its corrosion current is generally lower, which indicates that compared with the corroded steel, the corrosion trend of the bare steel is greater, but at the initial stage of immersion, the passivation film on the metal surface diffused slowly after dissolution, that is, the corrosion rate is controlled by the mass transfer process of the anodic dissolved products. For the corroded specimens of the three kinds of steels, with the prolongation of the corrosion period, the corrosion potential decreased first and then slightly increased, while the corrosion current gradually decreased. This shows that with the formation of a stable corrosion rust layer, the corrosion rate is getting smaller and smaller, and the rust layer can form an effective resistance to prevent further corrosion.

From the point of view of corrosion time, compared with Sb/Sn-free steel, Sb steel, and Sb + Sn steel, the corrosion phenomena of three kinds of bare steel are similar. At the initial stage of corrosion (24 and 72 h), the corrosion current of Sb + Sn steel is larger, and the corrosion rate is faster in the early stage. In the middle and late stages of corrosion (120 and 168 h), the corrosion current density of Sb + Sn steel, Sb steel without Sb/Sn steel, and the corrosion rate of Sb + Sn steel is significantly reduced. This shows that the early corrosion of weathering steel containing Sb and Sn elements is accelerated, which can promote the formation of a stable rust layer earlier.

Figure 13 shows the electrochemical Nyquist diagram impedance spectra of the three experimental steels after 168 h corrosion. The electrochemical impedance spectrum of bare steel is composed of incomplete semicircles in the high-frequency region and more complete semicircles in the low-frequency region. The radius of the semicircles reflects the size of the specimen impedance. The larger the radius, the larger the impedance and the better the protection performance of the rust layer. In general, the resistance of the rust layer dominates in the high-frequency region, and the charge transfer resistance at the rust interface dominates in the low-frequency region. There is no rust layer in the bare steel, so the reference value of the rust layer resistance in the high-frequency region is small, and the charge transfer resistance in the high-frequency region should be the main. As can be seen from Fig. 13a, the semi-circle radius of non-Sb/Sn steel is the largest in the low-frequency region, the semi-circle radius of Sb steel is in the middle, and the semi-circle radius of Sb + Sn steel is the smallest in the low-frequency region, which also indicates that the addition of Sb and Sn elements in the early

Table 5. Impedance spectrum parameters fitted by the equivalent circuit of Fig. 14

Time (h)	R_s (Ω cm^2)	C_r (μF cm^{-2})	R_r (Ω cm^2)	C_{dl} (μF cm^{-2})	R_t (Ω cm^2)	R_w (Ω cm^2)
Sb/Sn free steel						
24	10.22	0.3369	8.86	0.1959	11.59	0.08726
72	9.76	0.2421	13.42	0.8161	12.50	0.05143
120	13.23	0.3358	11.50	0.1344	12.17	0.05866
168	12.77	0.3434	15.59	0.1559	11.10	0.06793
Sb steel						
24	9.13	0.3829	9.28	0.2355	10.34	0.11260
72	11.19	0.1993	8.85	0.7825	13.82	0.04267
120	9.61	0.4578	13.31	0.3851	7.35	0.02476
168	13.54	0.3332	19.21	0.1246	9.92	0.08723
Sb + Sn steel						
24	8.91	0.3697	8.57	0.5012	3.726	0.08454
72	11.62	0.3311	9.29	0.2015	8.777	0.07919
120	15.36	0.2212	16.65	0.1038	13.11	0.06375
168	13.48	0.3338	21.32	0.2523	8.384	0.06591

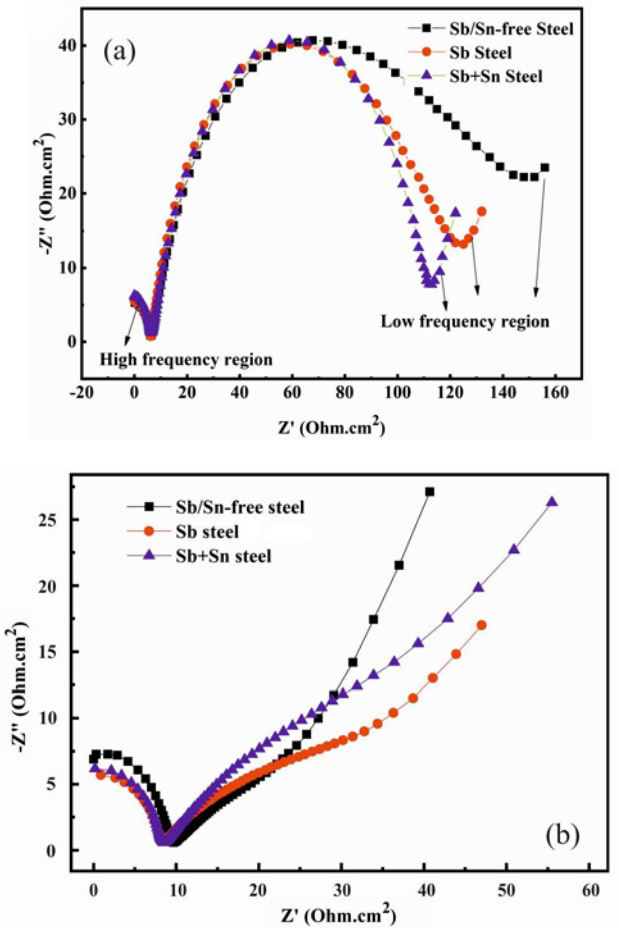

Fig. 13. Three kinds of experimental bare steel and Nyquist diagram after corrosion for 168 h: (a) bare steel and (b) corrosion for 168 h.

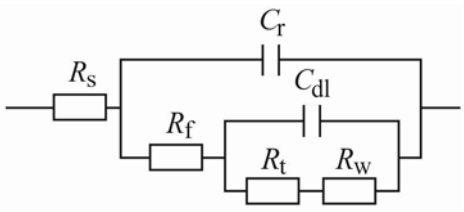

Fig. 14. Equivalent circuit of EIS data of the rusty sample.

corrosion stage can accelerate the early corrosion rate of weather-resistant steel, which is also consistent with the discussion results of polarization curve. Figure 13b shows the Nyquist diagram of three weathering steels corroded for 168 h.

The electrochemical impedance spectra of all corroded samples consist of incomplete semicircles in the high-frequency region and long tails in the low-frequency region, and the radius of the high-frequency region can evaluate the resistance of the rust layer. In the late corrosion stage, after 168 h, the resistance of the rust layer is the most useful for evaluating the protection performance of the rust layer, so the radius of the incomplete semicircle in the high-frequency region is mainly looked at. The radii of the high-frequency region of Sb + Sn steel and Sb steel are similar, and the radii of the high-frequency region of Sb + Sn steel are relatively large, indicating that the resistance of the rust layer is the largest and the protection effect is the strongest.

As shown in Fig. 14, *ZsimDemo software* was used to conduct equivalent circuit modeling for all Nyquist data [29, 30], and the parameters of the fitting results were listed in Table 5. R_s is the resistance of the so-

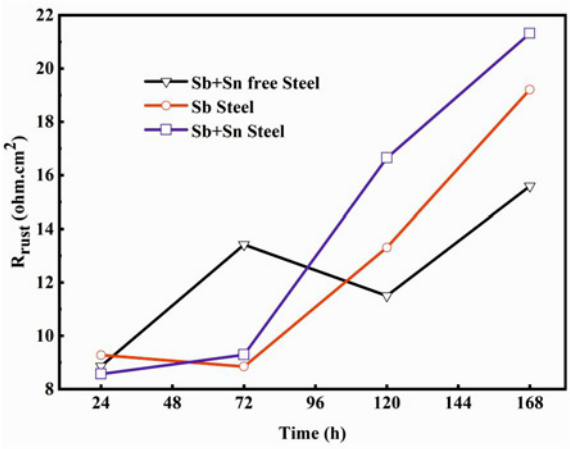

Fig. 15. The change of R_r of rusty samples with time.

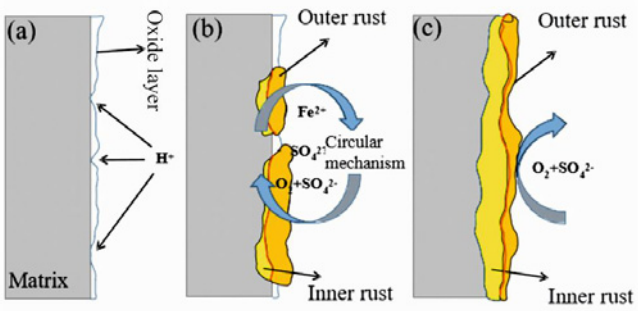

Fig. 16. Corrosion mechanism diagram of rust layer formation process: (a) early stage of corrosion, (b) middle stage of corrosion, and (c) later stage of corrosion.

lution, R_r is the resistance of the rust layer, C_r is the capacitance of the rust layer, C_{dl} is the capacitance of the double layer, R_t is the charge transfer resistance, and R_w is the impedance of diffusion.

The resistance (R_r) of the rust layer is most useful for estimating the protective properties of the rust layer [31]. According to the fitting parameters, the fitting value of R_r of the rusty sample with exposure time is shown in Fig. 15. With the increase of corrosion time, the rust layer resistance of the three kinds of steel is gradually increasing. In the early stage of corrosion 72 h, the rust layer resistance of Sb steel and Sb + Sn steel is only 8.85 and 9.29 Ω, which is significantly lower than the 13.42 Ω of steel without Sb/Sn. The rust layer impedance of Sb steel and Sb + Sn steel increases significantly at 120–168 h, and the rust layer impedance sequence is as follows: Sb + Sn steel > Sb steel > Sb/Sn free steel. On the one hand, the oxides of Sb and Sn (Sb_2O_5, SnO_2) are filled on the corrosion microcracks, which improves the density of the corrosion rust layer. On the other hand, Sb and Sn elements can accelerate the corrosion rate in the early stage and can quickly form a stable rust layer in the later stage of corrosion.

3.6. Corrosion mechanism

Complex chemical reactions occur during the cyclic infiltration corrosion test. During the wetting process, the anode mainly dissolves the steel, and the cathode mainly dissolves the O_2. During the drying process, conversion between corrosion products mainly occurs [32].

During the wetting process:
anode reaction

$$Fe \rightarrow Fe^{2+} + 2e; \quad Fe^{2+} \rightarrow Fe^{3+} + e, \tag{1}$$

cathode reaction

$$O_2 + 2H_2O + 4e \rightarrow 4OH^-, \tag{2}$$

during the drying process

$$Fe(OH)_3 \rightarrow FeOOH + H_2O. \tag{3}$$

The corrosion mechanism of the stable rust layer formation process is shown in Fig. 16. In the initial corrosion stage, point defects on the steel surface (Fig. 16a) preferentially corrode under the action of H^+, and unstable $Fe(OH)_3$ will be produced during the corrosion process, and $Fe(OH)_3$ is easily converted into α-FeOOH and γ-FeOOH in the rust layer. In the middle stage of corrosion, a thin electrochemical corrosion film will be formed on the surface of steel under the condition of infiltration, and HSO_3^- ions in the film will be continuously oxidized to SO_4^{2-}, which will then combine with Fe^{2+} to form a "SO_4^{2-} cycling mechanism", as shown in Fig. 16b, which is reflected as follows [28]:

$$HSO_3^- + \frac{1}{2}O_2 \rightarrow SO_4^{2-} + H^+, \tag{4}$$

$$Fe^{2+} + SO_4^{2-} + xH_2O \rightarrow FeSO_4 \cdot xH_2O, \tag{5}$$

$$FeSO_4 \cdot xH_2O + O_2 + (6-x)\,H_2O \rightarrow 4FeOOH + 4H_2SO_4, \tag{6}$$

$$2H_2SO_4 + O_2 + 2Fe \rightarrow FeSO_4 + 2H_2O. \tag{7}$$

At this time, the combination between the inner and outer rust layers is not tight, usually there are cracks between the inner and outer rust layers, and the thickness of the outer rust layer is greater than the thickness of the inner rust layer, and the loose and porous outer rust layer cannot protect the matrix. At the later stage of corrosion, as shown in Fig. 16c, the outer rust layer gradually falls off with the periodic infiltration experiment, while the inner rust layer

can be closely bonded with the matrix and gradually thickened. The increase of α-FeOOH content in the inner rust layer and the improvement of the density and stability of the rust layer can effectively prevent corrosive ions and oxygen from further invading the matrix, thus protecting the matrix. This is consistent with the decrease of corrosion weight loss and corrosion rate in the later stage of corrosion.

As we all know, the inner rust layer generated in the corrosion process is relatively dense, but there will also be small cracks. The oxides generated by Sb and Sn elements can fill the micro cracks, further improving the density of the inner rust layer. This is also an important reason for the rapid formation of a stable rust layer in the later stage of corrosion.

4. Conclusions

In this paper, a new generation of high-strength weathering steel was developed by adjusting the element ratio. By simulating the industrial atmospheric corrosion environment, the corrosion mechanism of high-strength weathering steel in $NaHSO_3$ solution was deeply discussed, and the role of Sb, Sn, and other elements in the rust layer was studied. The main conclusions are as follows:

1. In the $NaHSO_3$ corrosion medium simulating an industrial atmospheric environment, the corrosion rate of the three experimental steels showed a decreasing trend with the extension of the experiment period, and the corrosion behavior of Sb steel and Sb + Sn steel was more similar. The corrosion rate of Sb + Sn steel is the highest in the early corrosion stage, and the corrosion rate is the lowest in the late corrosion stage. Sb and Sn can accelerate the formation of a protective rust layer and make the rust layer denser.

2. The oxides in the three steel rust layers are mainly Fe_2O_3, Fe_3O_4, α-FeOOH, and γ-FeOOH. With the increase of corrosion time, the relative content of Fe_2O_3, Fe_3O_4, and γ-FeOOH gradually decreased, while the relative content of α-FeOOH gradually increased, and the performance of Sb + Sn steel was the most obvious, followed by Sb steel, and both Sb and Sn elements were conducive to promoting the generation of α-FeOOH. Sb and Sn are uniformly distributed in the rust layer and play an important role in improving the density of the rust layer.

3. From the electrochemical point of view, at the initial corrosion stage, the corrosion tendency of Sb + Sn steel is the largest, and the rust layer resistance is small. In the later stage of corrosion, the corrosion current density of Sb + Sn steel is the smallest, the resistance of the rust layer is obviously increased, and the formed rust layer is the most protective.

Acknowledgements

This work was financially supported by the High-quality Scientific Research Cultivation Project of Bengbu University (Grant No. 2021pyxm03), the Natural Science Foundation of the Higher Education Institutions of Anhui Province (Grant No. KJ2021A1118), the Provincial Quality Engineering Project of Anhui Universities (Grant No. 2022zygzts066), and The Discipline (Major) Leadership Development Program of Anhui Province (DTR2023057).

References

[1] M. Morcillo, I. Diaz, B. Chico, H. Cano, D. de la Fuente, Weathering steels: From empirical development to scientific design: A review, Corros. Sci. 83 (2014) 6–31. https://doi.org/10.1016/j.corsci.2014.03.006

[2] X. Zhang, S. Yang, W. Zhang, H. Guo, X. He, Influence of outer rust layers on corrosion of carbon steel and weathering steel during wet-dry cycles, Corros. Sci. 82 (2014) 165–172. https://doi.org/10.1016/j.corsci.2014.01.016

[3] Y. S. Choi, J. J. Shim, J. G. Kim, Effects of Cr, Cu, Ni and Ca on the corrosion behavior of low carbon steel in synthetic tap water, J. Alloy. Compd. 391 (2005) 162–169. https://doi.org/10.1016/j.jallcom.2004.07.081

[4] Z. Wang, J. Liu, L. Wu, R. Han, Y. Sun, Study of the corrosion behavior of weathering steels in atmospheric environments, Corros. Sci. 67 (2013) 1–10. https://doi.org/10.1016/j.corsci.2012.09.020

[5] Y. M. Fan, W. Liu, S. M. Li, T. Chowwanonthapunya, B. Wongpat, Y. G. Zao, B. J. Dong, T. N. Zhang, X. G. Li, Evolution of rust layers on carbon steel and weathering steel in high humidity and heat marine atmospheric corrosion, J. Mater. Sci. Technol. 39 (2020) 190–199. https://doi.org/10.1016/j.jmst.2019.07.054

[6] M. Morcillo, B. Chico, I. Diaz, H. Cano, D. de la Fuente, Atmospheric corrosion data of weathering steels: A review, Corros. Sci. 77 (2013) 6–24. https://doi.org/10.1016/j.corsci.2013.08.021

[7] W. Wu, X. Cheng, H. Hou, B. Liu, X. Li, Insight into the product film formed on Ni-advanced weathering steel in a tropical marine atmosphere, Appl. Surf. Sci. 436 (2018) 80–89. https://doi.org/10.1016/j.apsusc.2017.12.018

[8] B. Shi, X. Shen, G. Liang, Y. Zhu, Q. Xu, The superhydrophobic coating with low-temperature dew point corrosion resistance on an acid-resistant steel substrate prepared by the electrodeposition method, Mater. Corros. 73 (2022) 903–917. https://doi.org/10.1002/maco.202112832

[9] X. Wang, Y. Gao, K. Li, J. Yan, Y. Li, J. Feng, Effect of yttrium on the corrosion behaviour of 09CrCuSb alloy in concentrated sulphuric acid, Corros. Sci. 69 (2013) 369–375. https://doi.org/10.1016/j.corsci.2013.01.005

[10] V. F. C. Lins, R. B. Soares, E. A. Alvarenga, Corrosion behaviour of experimental copper-antimony-molybdenum carbon steels in industrial and marine atmospheres and in a sulphuric acid aqueous solution, Corros. Eng. Sci. Techn. 52 (2017) 1–7. https://doi.org/10.1080/1478422X.2017.1305537

[11] W. Xu, E. H. Han, Z. Wang, Effect of tannic acid on corrosion behavior of carbon steel in NaCl solution, J. Mater. Sci Technol. 35 (2019) 64–75. https://doi.org/CNKI:SUN:CLKJ.0.2019-01-010
[12] S. H. Ahn, K. J. Park, K. N. Oh, S. D. Hwang, B. J. Park, H. S. Kwon, M. Y. Shon, Effects of Sn and Sb on the corrosion resistance of AH 32 steel in a cargo oil tank environment, Met. Mater. Int. 21 (2015) 865–873. https://doi.org/10.1007/s12540-015-5164-5
[13] N. D. Nam, M. J. Kim, Y. W. Jang, J. G. Kim, Effect of tin on the corrosion behavior of low-alloy steel in an acid chloride solution, Corros. Sci. 52 (2010) 14–20. https://doi.org/10.1016/j.corsci.2009.08.036
[14] S.-H. Kim, S.-A. Park, J.-G. Kim, K.-S. Shin, Y. He, Alloying effect of copper on the corrosion properties of low-alloy steel for flue gas desulfurization system, Met. Mater. Int. 21 (2015) 232–241. https://doi.org/10.1007/s12540-015-4090-x
[15] Q.-H. Zhao, W. Liu, J.-W. Yang, Y.-C. Zhu, B.-L. Zhang, M.-X. Lu, Corrosion behavior of low alloy steels in a wet-dry acid humid environment, Int. J. Min. Met. Mater. 2016, 23 (2016) 9–20. https://doi.org/10.1007/s12613-016-1325-x
[16] D. P. Le, W. S. Ji, J. G. Kim, K. J. Jeong, S. H. Lee, Effect of antimony on the corrosion behavior of low-alloy steel for flue gas desulfurization system, Corros. Sci. 5 (2008) 1195–1204. https://doi.org/10.1016/j.corsci.2007.11.027
[17] B. Y. Wu, W. Liang, A. H. Wang, Compositional design of low carbon sulphuric acid dewpoint corrosion resistant steel and corresponding anticorrosive mechanism, British Corrosion Journal 48 (2013) 313–320. https://doi.org/10.1179/1743278212Y.0000000071
[18] S. A. Park, S. H. Kim, Y. H. Yoo, J. G. Kim, Effect of chloride ions on the corrosion behavior of low-alloy steel containing copper and antimony in sulfuric acid solution, Met. Mater. Int. 21 (2015) 470–478. https://doi.org/10.1007/s12540-015-4421-y
[19] V. F. C. Lins, R. B. Soares, A. E. Alvarenga, Corrosion behaviour of experimental copper-antimony-molybdenum carbon steels in industrial and marine atmospheres and in a sulphuric acid aqueous solution, Corros. Eng. Sci. Techn. 52 (2017) 397–403. https://doi.org/10.1080/1478422x.2017.1305537
[20] D. Kowalski, M. Ueda, T. Ohtsuka, Corrosion protection of steel by bi-layered polypyrrole doped with molybdophosphate and naphthalenedisulfonate anions, Corros. Sci. 49 (2007) 1635–1644. https://doi.org/10.1016/j.corsci.2006.08.018
[21] Y. H. Qian, C. H. Ma, D. Niu, J. Xu, M. Li, Influence of alloyed chromium on the atmospheric corrosion resistance of weathering steels, Corros. Sci. 74 (2013) 424–429. https://doi.org/10.1016/j.corsci.2013.05.008
[22] Y. Jia, M. Yang, W.-E. Lu, F. Ji, C.-B. Li, Y.-T. Fang, Y. Xia, Anti-corrosion property of atomic layer deposition films for anodized aluminum, Mater. Sci. For. 809 (2014) 689–694. https://doi.org/10.4028/www.scientific.net/MSF.809-810.689
[23] E. Matsubara, S. Suzuki, Y. Waseda, Corrosion Mechanism of Iron from an X-ray. in: Y. Waseda, S. Suzuki (Eds.), Structural Viewpoint, in Characterization of Corrosion Products on Steel Surfaces, Springer, Berlin, 2006, pp. 105–129. https://doi.org/10.1007/978-3-540-35178-8_6
[24] M. Yamashita, H. Konishi, T. Kozakura, J. Mikuzi, H. Uchida, In situ observation of initial rust formation process on carbon steel under Na_2SO_4 and NaCl solution films with wet/dry cycles using synchrotron radiation X-rays, Corros. Sci. 47 (2005) 2492–2498. https://doi.org/10.1016/j.corsci.2004.10.021
[25] B. Wang, Z.-T. Li, D.-P. Zhan, M.-F. Jiang, Precipitation behavior of VN in high nitrogen and vanadium micro-alloyed low carbon weathering steel, T. Indian I. Metals 71 (2018) 1607–1613. https://doi.org/10.1007/s12666-018-1295-y
[26] Z. J. Xie, X. P. Ma, C. J. Shang, Nano-sized precipitation and properties of a low carbon niobium microalloyed bainitic steel, Mater. Sci. Eng. A 641 (2015) 37–44. https://doi.org/10.1016/j.msea.2015.05.101
[27] J. Li, J. Wu, Z. Wang, S. Zhang, X. Wu, Y. Huang, X. Li, The effect of nanosized NbC precipitates on electrochemical corrosion behavior of high-strength low-alloy steel in 3.5%NaCl solution, Int. J. Hydrogen. Energ. 42 (2017) 22175–22184. https://doi.org/10.1016/j.ijhydene.2017.03.087
[28] Z. Song, T. Guo, Y. Zhang, X. Nan, X. Xu, Z. Dong, The corrosion behavior of weathering bridge steel with oxide scale in different corrosion environments, Surf. Topogr. Metrol. Prop. 8 (2020) 025004. https://doi.org/10.1088/2051-672X/ab8502
[29] J. H. Wang, F. I. Wei, Y. S. Chang, H. C. Shih, The corrosion mechanisms of carbon steel and weathering steel in SO_2 polluted atmospheres, Mater. Chem. Phys. 47 (1997) 1–8. https://doi.org/10.1016/S0254-0584(97)80019-3
[30] L. Hao, S. Zhang, J. Dong, W. Ke, Evolution of atmospheric corrosion of MnCuP weathering steel in a simulated coastal-industrial atmosphere, Corros. Sci. 59 (2012) 270–276. https://doi.org/10.1016/j.corsci.2012.03.010
[31] K. Asami, M. Kikuchi, In-depth distribution of rusts on a plain carbon steel and weathering steels exposed to coastal-industrial atmosphere for 17 years, Corros. Sci. 45 (2003) 2671–2688. https://doi.org/10.1016/S0010-938X(03)00070-2
[32] D. D. N. Singh, S. Yadav, J. K. Saha, Role of climatic conditions on corrosion characteristics of structural steels, Corros. Sci. 50 (2008) 93–110. https://doi.org/10.1016/j.corsci.2007.06.026